

# Effect of Atmospheric propagation of Electromagnetic Wave on DInSAR Phase †

Preethi Malur Balaji <sup>1,2</sup> and Shashi Kumar <sup>1,\*</sup>

<sup>1</sup> Indian Institute of Remote Sensing, Indian Space Research Organization, Dehradun 248001, India; preet.balaji20@gmail.com

<sup>2</sup> ITC, Faculty of Geoinformation Science and Earth Observation, University of Twente, 7500 Enschede, The Netherlands

\* Correspondence: shashi@iirs.gov.in; Tel.: +91-135-2524119

† Presented at the 3rd International Electronic Conference on Remote Sensing, 22 May–5 June 2018; Available Online: <https://sciforum.net/conference/ecrs-3>

Published: 22 May 2019

**Abstract:** Earth's topography and deformation mapping have become easier by the use of a geodetic technique popularly known as repeat-pass Synthetic Aperture Radio Detection and Ranging (SAR/RADAR) Interferometry (InSAR). However, the measurements obtained through InSAR are liable to atmospheric errors. Water vapor and clouds present in the troposphere and the Total Electron Content (TEC) of the ionosphere are responsible for the additional path delay in the wave. An increase is induced in the observed range due to tropospheric refractivity and path shortenings are observed due to ionospheric electron density. The quality of phase measurement is affected by these atmospheric induced propagation delays and hence errors are introduced in the topography and deformation fields. A three-pass differential synthetic aperture radar interferometry (DInSAR) is performed from two interferograms and the effect of this atmospheric delay is studied on the same study area. The interferograms are generated from three single look complex (SLC) phased array type L-band synthetic aperture radar (PALSAR) data of advanced land observing satellite (ALOS). Atmospheric phase correction is done on the generated DInSAR and it is found that atmospheric error correction is essential in order to avoid inaccurate erratic height and deformation measurements.

**Keywords:** DInSAR; topographic phase; ionospheric phase; atmospheric delay; differential interferogram; total electron content

---

## 1. Introduction

Synthetic aperture radar (SAR) as an extensive tool uses SAR interferometry (InSAR) which is a processing technique to measure the topography of the surface, its changes over time, and also other changes in the surface. It is a technique in which two SAR images are combined to produce an interferogram. An interferogram is a phase interference image. In SAR interferometry, the deformation signal obtained from the Earth surface is mixed with topographic signal. To overcome this problem, a differential interferogram is used. A three-pass differential synthetic aperture radar interferometry or DInSAR is used in remote sensing for measuring Earth surface deformation [1,2]. When two interferograms are formed from three single look complex (SLC) images, the interferogram phases are again differenced to form one more interferogram which is termed as "Double-Differenced Interferogram" [3]. This step removes phase changes due to topography and a new phase image is formed. The final phase of the DInSAR consists of surface change phase contributions, atmospheric delay contribution, and phase noise [4]. The atmospheric effects which contribute to phase differences cannot be easily distinguished from surface displacements. The effect of atmospheric contributions

has an impact on altitude and surface deformation measurements [5,6]. The approach adopted in this work is shown in the flow diagram of methodology as shown in Figure 1.

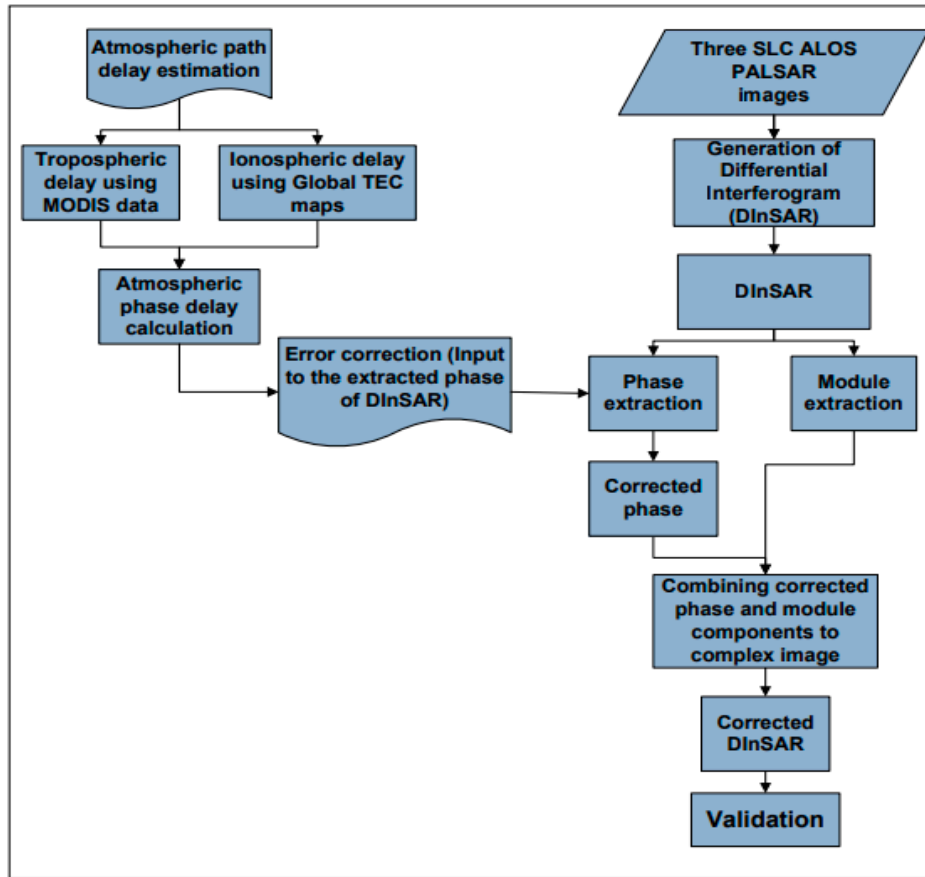


Figure 1. Methodology.

## 2. Effects of Atmospheric Propagation

The atmosphere is divided into two major layers, ionosphere and troposphere. These layers affect the propagation of electromagnetic waves, due to their different refractive indices. The path delay due to troposphere which is the lowest portion of the Earth’s atmosphere is caused due to air refractivity gradients. The two-way incremental path length  $\Delta R_e$  (m) can be approximated by integrating the parameters (temperature, pressure and partial pressure of water vapor) over the total path length in the troposphere [7], as seen in Equation (1).

$$\Delta R_e = 2 \times 10^{-6} \int_0^H \frac{N}{\cos\theta} dh, \tag{1}$$

where  $H$  is the vertical distance travelled by the RADAR wave in m,  $N$  is the refractivity,  $\theta$  is the incidence angle and  $h$  is the topographic height.

On the other hand, the ionosphere is characterized by free electrons that are created by external sources such as ultraviolet radiation from the Sun. These external sources create free electrons by knocking them off from atoms. The two-way path delay ( $\Delta s$ ) occurred while the RADAR wave propagates through the ionosphere as given by [8] is described in Equation (2)

$$\Delta s = 2 \times K \times \frac{TEC}{f^2 \cos \alpha_{\text{offnadir}}}, \tag{2}$$

where  $K$  is the refractivity constant which corresponds to  $-40.28 \text{ m}^3 \text{ s}^{-2}$ ,  $f$  is the frequency of the L-band wave which is 1.276 GHz,  $\alpha_{\text{offnadir}}$  is the Satellite Offnadir angle corresponding to  $34.3^\circ$  and

Total Electron Content (TEC) is derived from the Global Ionospheric Map produced by Centre for Orbit Determination in Europe (CODE), as shown in Figure 2. In the figure, the red curve shows the mean TEC, a trend function is plotted in blue, and the black dots indicate the daily average mean TEC. The daily mean TEC for the months of Master, Slave 1, and Slave 2 image acquisitions are derived from this map.

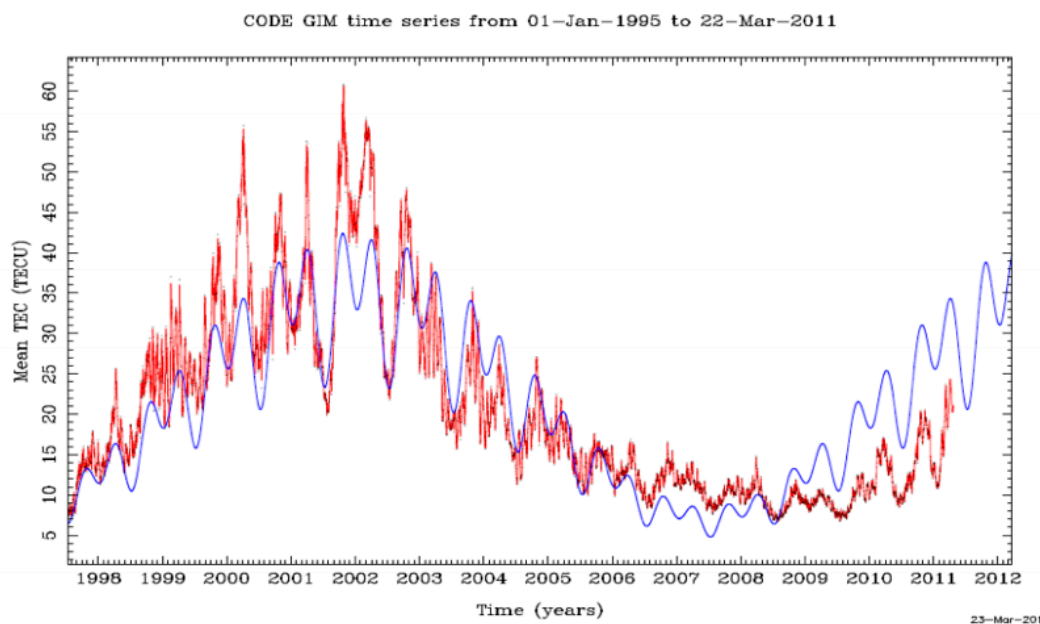


**Figure 2.** Total Electron Content (TEC) map showing yearly and monthly TEC variations.

The electron density in the ionosphere creates propagation path shortenings and the partial pressure of water vapor in troposphere causes an increase in the observed range.

### 3. DInSAR Generation from the Two Interferograms

The two processes that are the generation of DInSAR and calculation of atmospheric path delay require two different datasets. DInSAR is generated using three Advanced Land Observation Satellite (ALOS) carrying Phased Array L-band Synthetic Aperture RADAR (PALSAR) L-band SLC images acquired on the same site. The images were acquired on June 16 (Master image), August 1 (Slave image 1), and September 16 (Slave image 2), 2010. To calculate the tropospheric path delay, the Moderate Resolution Imaging Spectroradiometer (MODIS) data acquired on the same study area for the same three dates were used. The site chosen for study swathes a part of the state Uttarakhand located in the northern part of India. This area was chosen for study particularly because of its varied land cover types. Different scatterers can be found as distributed scatterers in this study area. The dense deciduous forests of Rajaji national park and Barkot forest range illustrate volume scattering. Permanent scatterers like buildings and mountains act as corner reflectors for the L-band RADAR wave. The water bodies having a smooth surface form the specular reflectors and the agricultural lands during crop growth act as volume scatterers, and when plain, act as a smooth surface for specular reflectance. All these properties put together to make the area a complete package to undertake research work.

The differential interferometric processing aims at separating the topographic and displacement terms in an interferogram. The topographic phase has to be removed to identify the displacement component. The three-pass DInSAR is based on three SAR images from which two interferometric pairs are formed having one master image in common. One of the pairs (topo-pair) is used to estimate the topographic phase which is considered to be the reference pair. The larger the perpendicular baseline, the more the sensitivity of the interferogram to topography is. Hence, the topo-pair should be acquired with a short acquisition time interval and a large interferometric baseline. This pair does not include the displacement (if any) to be investigated. The other pair (defo-pair) in general consists

of one image before and one image after the coherent displacement. This pair should be acquired with a baseline as small as possible.

The three-pass DInSAR method is illustrated in Figure 3. The solid lines in the figure show the RADAR signal paths for the first interferogram pair formed by antennas at locations  $A_1$  and  $A_2$  and the dashed lines show the signal path for the second interferometric pair acquired over the same site with antennas located at positions  $A_1$  and  $A'_2$ .  $\rho$ ,  $(\rho + \delta\rho)$  and  $(\rho + \delta\rho')$  are the path lengths measured from  $A_1$ ,  $A_2$ , and  $A'_2$  respectively,  $\lambda$  is the wavelength of the RADAR wave,  $B_{||}, B'_{||}$  are the components of the baseline parallel to the look direction of the first pair and second pair respectively,  $B, B'$  are baseline lengths of the first pair and second pair respectively,  $\theta$  is the look angle, and  $\alpha, \alpha'$  are the angle of the baseline with respect to horizontal at the sensor for the first pair and second pair respectively.

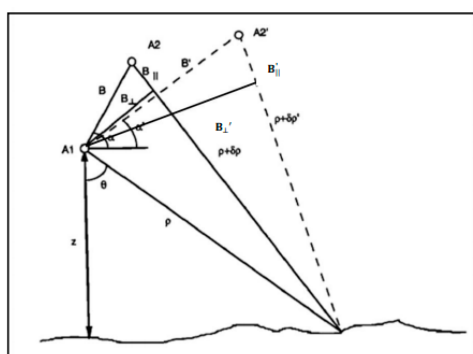


**Figure 3.** Three-pass differential synthetic aperture radar interferometry (DInSAR) method.

The flattened interferogram is equal to the product of the perpendicular component of the baseline  $B_{\perp}$  and topographic angular distortion  $\delta\theta$ . From Figure 3, the ratio of the two phases could be written as [9]:

$$\frac{\Phi_{flat}}{\Phi'_{flat}} = \frac{B_{\perp}}{B'_{\perp}} \tag{3}$$

In order to remove the topographic term and retain only the displacement term in the DInSAR, the data from the first interferogram are scaled to the perpendicular baseline conditions of the second interferogram and subtracted from it. This eliminates the confusion created between the topographic term and displacement term during the interpretation of results.

The differential phase equation is given by [9]

$$\Phi_{flat} - \frac{B_{\perp}}{B'_{\perp}} \Phi'_{flat} = \frac{4\pi}{\lambda} \Delta\rho, \tag{4}$$

where  $\Delta\rho$  is the displacement term,  $\lambda$  is the wavelength of the radar wave,  $\Phi_{flat}$  and  $\Phi'_{flat}$  are the flattened interferograms generated from the first and second pair respectively and  $B_{\perp}$  and  $B'_{\perp}$  are the perpendicular baseline components of the first and second pair respectively.

#### 4. Phase Correction

The three-pass DInSAR is generated using three single look complex (SLC) phased array type L-band synthetic aperture radar (PALSAR) data of advanced land observing satellite (ALOS). The phase correction is done on the generated DInSAR using the range correction already calculated [9].

$$\Phi - \Psi_{\text{correction1}} = \frac{4\pi}{\lambda} \delta\rho, \tag{5}$$

$$\Phi' - \Psi_{\text{correction2}} = \frac{4\pi}{\lambda} \delta\rho', \tag{6}$$

where,  $\frac{4\pi}{\lambda} \delta\rho$  and  $\frac{4\pi}{\lambda} \delta\rho'$  represent the corrected phase of the two interferograms.

## 5. Results and Discussion

### 5.1. Path Delay Occurred

The tropospheric delay for the Slave image 1 and Slave image 2 was found to range between 2 and 10 m. For the master image, not much variation in the tropospheric delay was reported. This is mainly due to the presence of less water vapor and clouds. Considerably less water vapor forming clouds are encountered in this region on this date, as this month is apparently dry albeit a delay of 7.6 to 7.8 m is noticed at some points in the region.

The ionospheric delay for the months of June, August, and September (Master image, Slave image 1 and Slave image 2 respectively) has been reported to be -5.39, -6.59, and -7.19 m, respectively. The negative sign of the delay indicates the phase advance.

The total delay caused due to troposphere and ionosphere is shown in the form of histograms shown in Figures 4–6.

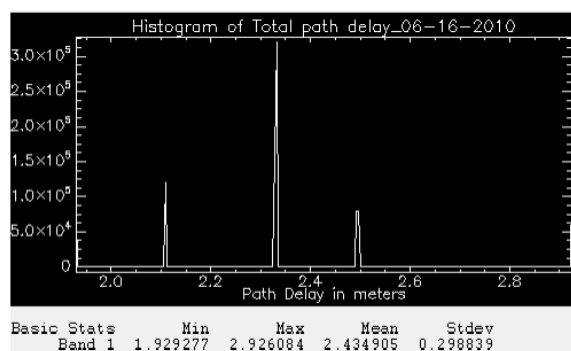


Figure 4. Total path delay due to atmospheric propagation of electromagnetic wave on June 16, 2010.

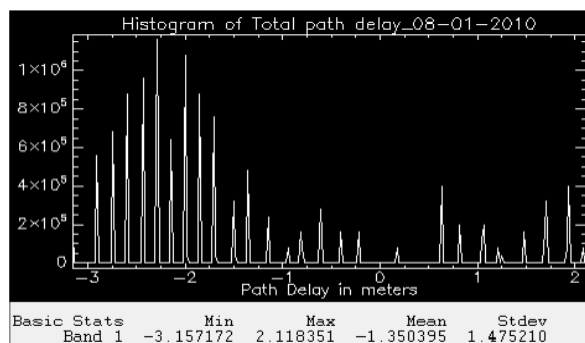
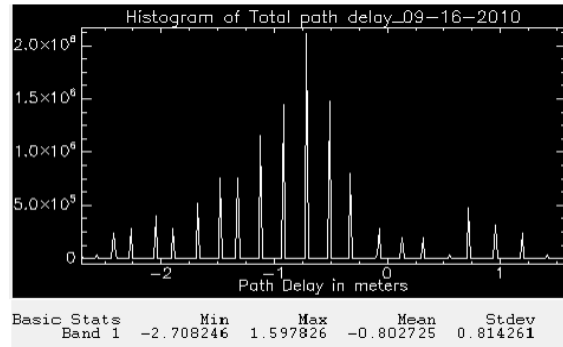


Figure 5. Total path delay due to atmospheric propagation of electromagnetic wave on August 1, 2010.



**Figure 6.** Total path delay due to atmospheric propagation of electromagnetic wave on September 16, 2010.

5.2. Correction on the Phase of DInSAR

Using Equations (5) and (6) mentioned in Section 4, the correction on the phase of the two interferograms generated from the three SLC images was performed. Using the two corrected interferograms, the DInSAR was generated. A comparison of the generated three-pass DInSAR before and after correction is shown in Figures 7 and 8.

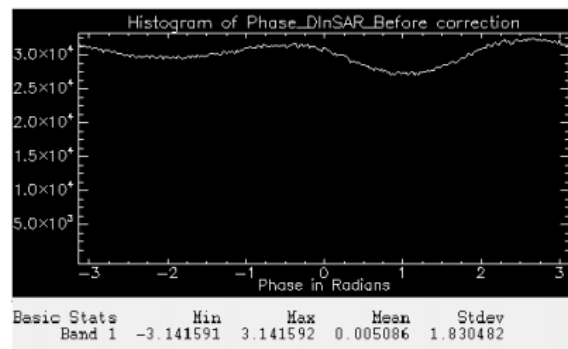


**Figure 7.** The DInSAR phase before correction.

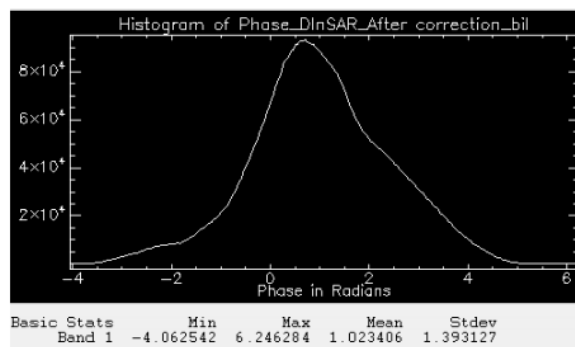


**Figure 8.** The DInSAR phase after correction.

The phase of DInSAR before correction as seen in Figure 7 shows a variation between  $-3$  and  $+3$  rad. After applying the correction, as seen in Figure 8, the phase values appear close to zero. The DInSAR which is an outcome of subtraction of two interferograms contains the displacement phase. According to a minor survey made on the study site, no changes in the land have been recorded and hence there is no displacement phase present in the DInSAR. Most of the phase as seen in the above figure has accumulated around zero. However, the phase is not exactly equal to zero. This is because

of the baseline decorrelation and presence of phase noise (error due to temporal decorrelation and volume scattering). The atmospheric correction has influenced the values of the DInSAR to a great extent. When the phase of the DInSAR before correction and phase of the DInSAR after correction are observed, a drastic change is noticeable. Before the correction, the phase as seen from Figure 7 shows random variation. Once the correction is applied, the phase values are altered and are brought back to a meaningful phase term.

The phase of the whole interferogram is compared with the phase of the region having high coherence. This is done by taking 100 points on the region having high coherence and the remaining area of study.

It is clear from Figures 7 and 8 that atmospheric error removal influences the DInSAR measurements to a significant extent. The changes in phase can be clearly noticed when the error correction is applied. In order to obtain reliable displacement measurements from a DInSAR, it is required to eliminate the atmospheric error. The main requirement of repeat-pass interferometry is coherence. If there is a coherence loss, this technique is not suitable for the height and displacement measurements.

The area of high coherence where no change has occurred on land shows the influence of error correction clearly. Once the correction is applied, the phase values close to zero are noticeable.

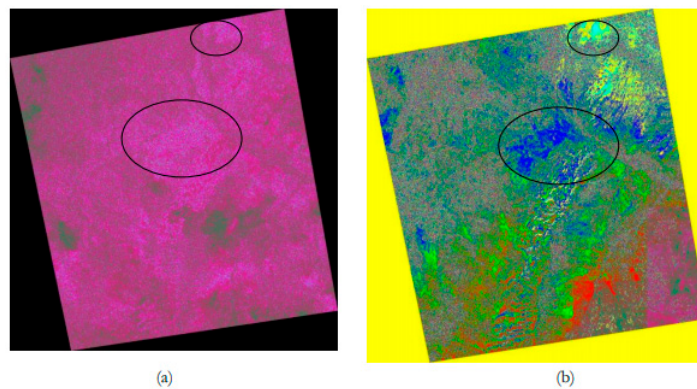


**Figure 9.** Differential interferogram; (a) before atmospheric correction; (b) after atmospheric correction.

Figure 9a,b shows the differential interferogram generated before and after atmospheric error removal. As seen in the above Figure 9 a,b, the Regions within the black circles are more clearly visible in the DInSAR after correction. This region is hardly seen in the DInSAR before correction. Also, many other regions such as the mountainous regions, plain lands etc. can be clearly seen after applying the correction in the DInSAR. A clear demarcation in the DInSAR before and after correction can be noticed from the above figures.

### 5.3. DInSAR Error Map

Figure 10 shows the amount of atmospheric error introduced in the DInSAR. This much error, when subtracted from the original DInSAR, gives the atmospheric corrected DInSAR. The maximum error introduced in the phase of the DInSAR is 7.9466 rad. This amount of error leads to inaccurate measurements.

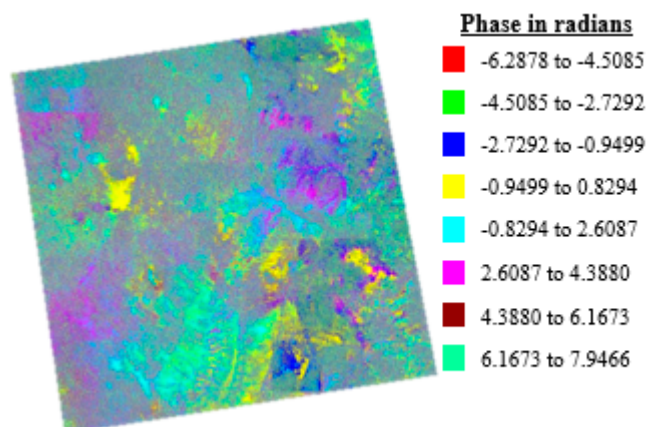


Figure 10. Atmospheric error map.

## 6. Conclusion

It can be concluded from this work that the atmospheric disturbances can hinder the InSAR measurements giving inaccurate results. The atmosphere has a major impact on the phase of a RADAR wave. Hence, it is essential to eliminate these errors from the phase of the interferogram to minimize the production of inaccurate measurements and thus make InSAR a powerful technique for height and ground displacement measurements.

**Conflicts of Interest:** The authors declare no conflict of interest.

## References

1. Babu, A. and Kumar, S. SBAS interferometric analysis for volcanic eruption of Hawaii island. *J. Volcanol. Geotherm. Res.* **2019**, *310*, 31–50.
2. Casu, F.; Manzo, M.; Lanari, R. A quantitative assessment of the SBAS algorithm performance for surface deformation retrieval from DInSAR data. *Remote Sens. Environ.* **2006**, *102*, 195–210.
3. Gabriel, A.K.; Goldstein, R.M.; Zebker, H.A. Mapping small elevation changes over large areas: Differential radar interferometry. *J. Geophys. Res. Solid Earth* **1989**, *94*, 9183–9191.
4. Lanari, R.; Casu, F.; Manzo, M.; Zeni, G.; Berardino, P.; Manunta, N.; Pepe, A. An overview of the Small BAseline Subset algorithm: A DInSAR technique for surface deformation analysis. *Pure Appl. Geophys.* **2007**, *164*, 637–661.
5. Zhou, X.; Chang, N.-B.; Li, S. Applications of SAR Interferometry in Earth and Environmental Science Research. *Sensors* **2009**, *9*, 1876–1912.
6. Gonnuru, P.; Kumar, S. PsInSAR based land subsidence estimation of Burgan oil field using TerraSAR-X data. *Remote Sens. Appl. Soc. Env.* **2018**, *9*, 17–25.
7. Hanssen, R.; Frijt, A. A First Quantitative Evaluation of Atmospheric Effects on SAR Interferometry. In Proceedings of the Fringe 96 Workshop, Zurich, Switzerland, 30 September–2 October 1996; p. 277.
8. Jehle, M.; Frey, O.; Small, D.; Meier, E.; Nüesch, D. Improved Knowledge of SAR Geometry through Atmospheric Modelling. University of Zurich. Available online: <https://pdfs.semanticscholar.org/12c6/2eb9d8c30c4c04965c9cd14acc99100d418b.pdf> (accessed on 14 September 2010)
9. Zebker, H.A.; Rosen, P.; Goldstein, R.M.; Gabriel, A.; Werner, C.L. On the derivation of coseismic displacement fields using differential radar interferometry: The Landers earthquake. *J. Geophys. Res. Solid Earth.* **1994**, *99*, 19617–19634.

